

Electronic Supplementary Information (ESI)

Metal-doped TiO₂ colloidal nanocrystals with broadly tunable plasmon resonance absorption

Sheng Cao^{a, b}, Shengliang Zhang^{a, b}, Tianran Zhang^{a, b}, Adrian Fisher^{b, c}, and Jim Yang Lee^{, a, b}*

^a Department of Chemical and Biomolecular Engineering, National University of Singapore, 10 Kent Ridge Crescent, Singapore 119260, Singapore

^b Cambridge Centre for Advanced Research and Education in Singapore, 1 Create Way, Singapore 138602, Singapore

^c Department of Chemical Engineering and Biotechnology, University of Cambridge, Pembroke Street, Cambridge CB2 3RA, United Kingdom

Corresponding Email: cheleejy@nus.edu.sg

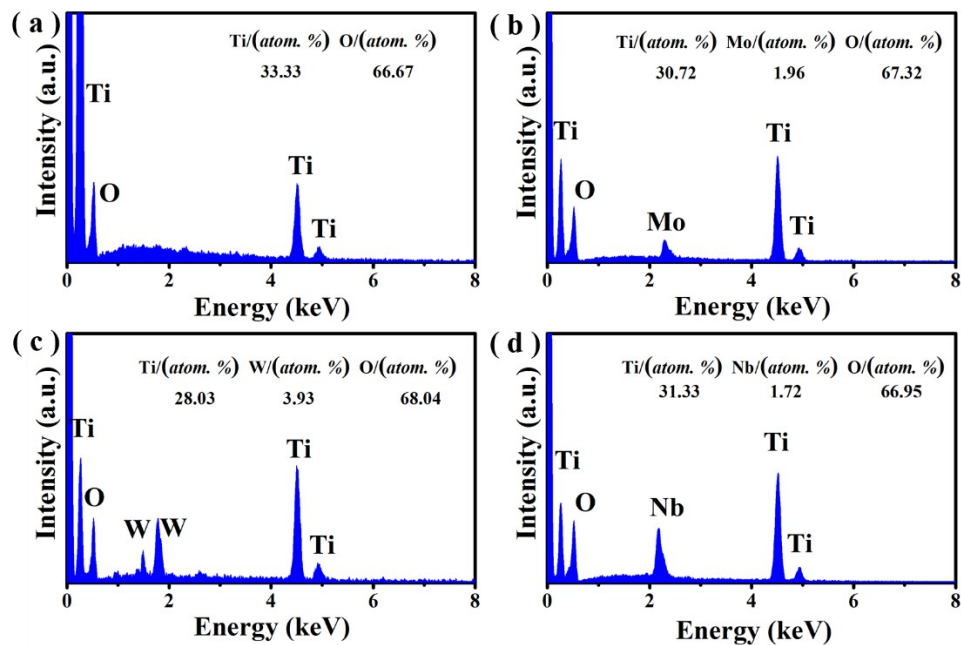


Fig. S1 Typical EDS spectra of (a) pristine TiO_2 , (b) Mo:TiO₂, (c) W:TiO₂, and (d) Nb:TiO₂ NCs. The insets show the corresponding chemical contents.

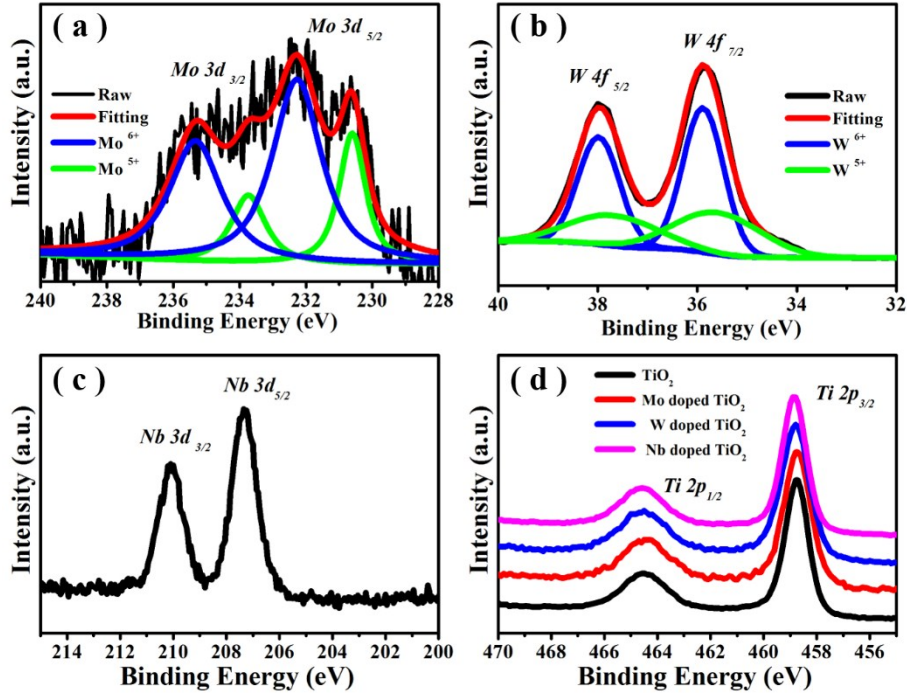


Fig. S2 XPS spectra of doped TiO_2 NCs: (a) Mo 3d, (b) W4f, (c) Nb 3d and (d) Ti 3p

Fig. S2a shows that the Mo 3d spectrum can be deconvoluted into two sets of doublets due to Mo $3d_{5/2}$ and Mo $3d_{3/2}$, with an intensity ratio of 3/2 and 3.2 eV apart. The doublet at 230.5 and 233.7 eV corresponds to the $Mo^{5+}\ 3d_{5/2}$ and $Mo^{5+}\ 3d_{3/2}$ states; and the doublet at 232.2 and 235.4 eV to the $Mo^{6+}\ 3d_{5/2}$ and $Mo^{6+}\ 3d_{3/2}$ states respectively. These measurements suggest the co-existence of two Mo oxidation states (27.4% Mo^{5+} and 72.6% Mo^{6+}).¹ Similarly, the W 4f spectrum in Fig. S2b can be deconvoluted into the $W\ 4f_{7/2}$ and $W\ 4f_{5/2}$ doublets, with an intensity ratio of 4/3 and 2.1 eV apart. The doublet at 35.6 and 37.7 eV is assignable to $W^{5+}\ 4f_{7/2}$ and $W^{5+}\ 4f_{5/2}$ while the doublet peaks at 35.8 and 37.9 eV to $W^{6+}\ 4f_{7/2}$ and $W^{6+}\ 4f_{5/2}$. The two W oxidation states in co-existence are 37.8% W^{5+} , and 62.2% W^{6+} .² Fig. S2c shows the Nb 3d spectrum with a doublet at 210.98 eV and 208.08 eV associated with Nb $3d_{3/2}$ and Nb $3d_{5/2}$, with a spin orbit splitting of 2.9 eV, confirming the presence of Nb^{5+} .³ Thus, the oxidation states of the dopant ions in TiO_2 ($Mo^{5+/6+}$, $W^{5+/6+}$, and Nb^{5+}) could all be identified by the XPS measurements.

Table S1. Chemical compositions of doped TiO₂ NCs as analyzed by EDS and XPS

Material	Nominal ratio (<i>atom %</i>)	Ratio from EDS (<i>atom %</i>)	Ratio from XPS (<i>atom %</i>)
Mo-doped TiO ₂	Mo/Ti=10	6.4	7.0
W-doped TiO ₂	W/Ti=10	13.5	16.7
Nb-doped TiO ₂	Nb/Ti=10	5.5	5.4

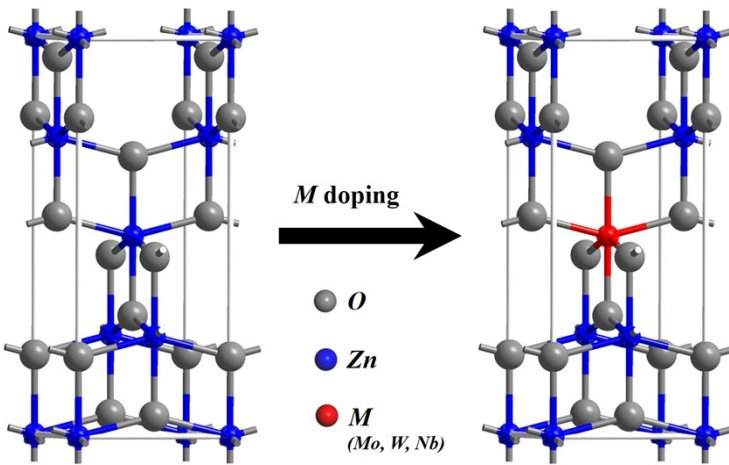


Fig. S3 Schematic of the substitutional metal (M) doping of the TiO_2 crystal lattice via the formation of solid solution.

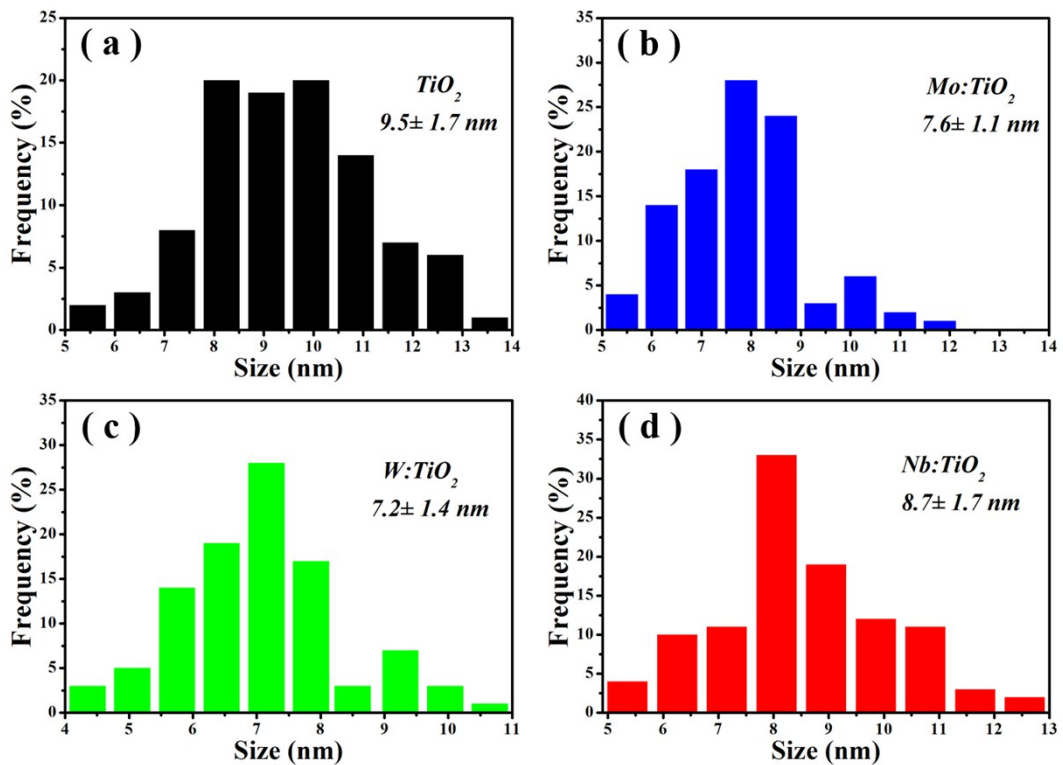


Fig. S4 Size distributions of pristine (a) TiO_2 , (b) $\text{Mo}:\text{TiO}_2$, (c) $\text{W}:\text{TiO}_2$, and (d) $\text{Nb}:\text{TiO}_2$ NCs.

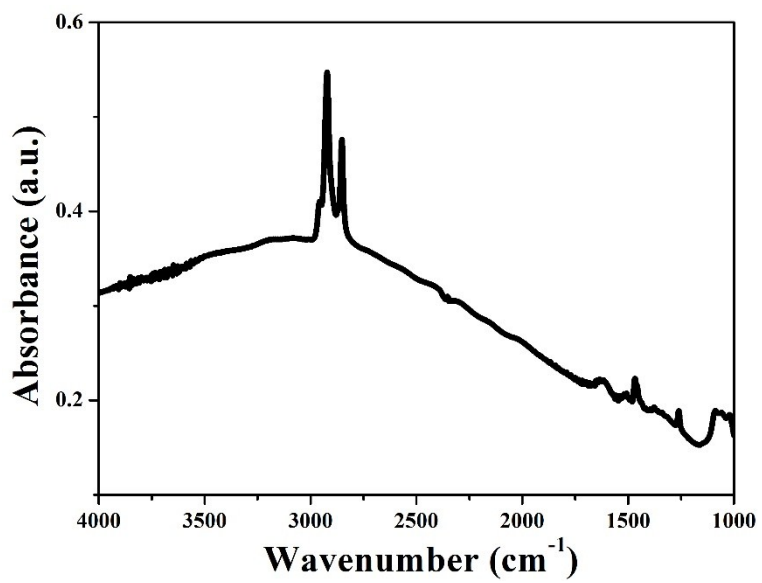


Fig. S5 Fourier-transform infrared spectrum (FTIR) of a Nb:TiO₂ NC film formed by drop-casting the Nb:TiO₂ NCs solution.

Conduction Band

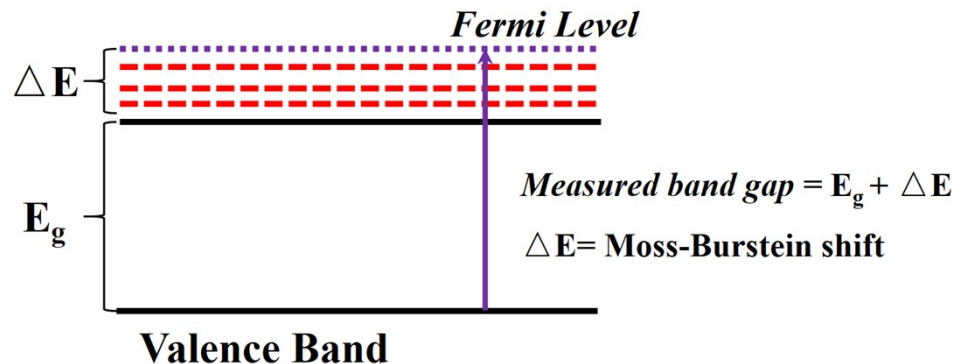


Fig. S6 Schematic diagram of the Burstein-Moss effect.⁴

The blue shift in the optical bandgap in heavily doped semiconductors is mainly caused by the Burstein-Moss effect, due to the high density of free electrons introduced by the dopant to populate the states close to the conduction band.⁵ As shown in Fig. S6, the apparent optical bandgap = actual bandgap + Moss-Burstein shift.⁴ If the conduction band edge of TiO₂ does not change with the dopant type, then the bandgap of the Mo-doped TiO₂ NCs with the highest electron density should be larger than the bandgaps of Nb-and W-doped TiO₂ NCs. However, the bandgap of M-doped TiO₂ can also be shifted by exchange interactions in the free-electron gas and electrostatic interactions between free electrons and the ionized impurities;⁶ and the extent of such interaction is dopant type dependent.⁷ This effect makes it difficult to directly compare between the optical spectra of Mo-, Nb- and W-doped TiO₂ NCs and to attribute the origin of the enlarged optical bandgap. The enlarged bandgaps in Fig. 3c are therefore used suggest the existence of Burstein-Moss effect in our doped NCs.

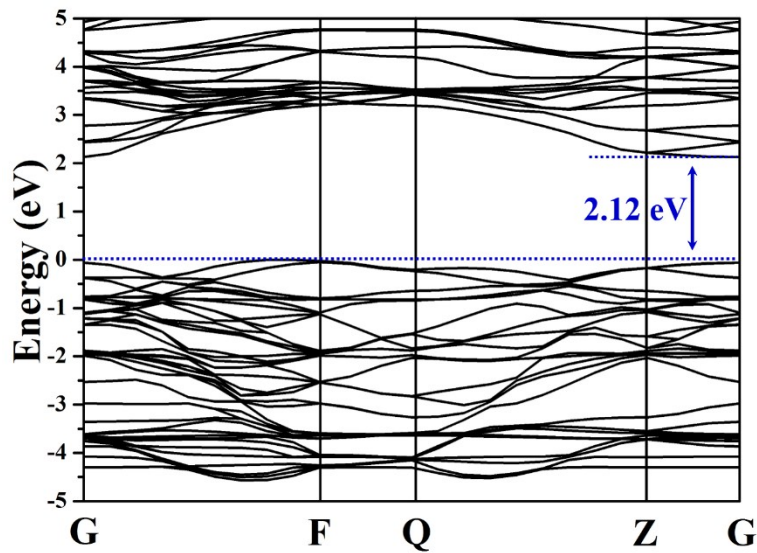


Fig. S7 The calculated band structure of pristine TiO_2 .

Table S2. Chemical compositions of W-doped TiO₂ NCs with different dopant levels as measured by EDS and XPS

Nominal W/Ti ratio (atom %)	Ratio W/Ti from EDS (atom %)	Ratio W/Ti from XPS (atom %)	Doping concentration from EDS (atom %)
1	1.5	2.6	1.5
2.5	3.9	5.3	3.8
5	6.1	8.7	5.7
10	13.5	16.7	11.9
15	17.9	21.2	15.2
20	24.2	27.4	19.5

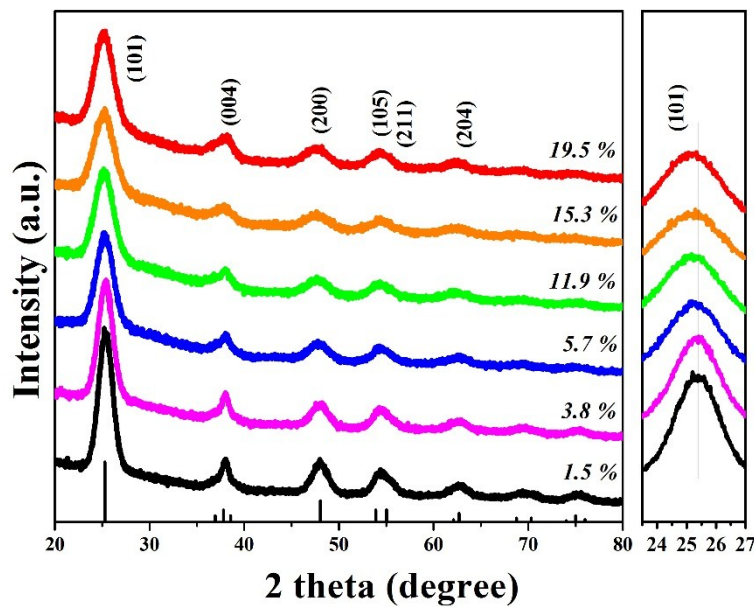


Fig. S8 XRD patterns of W-doped TiO₂ NCs with different W-concentrations. The expanded view of the TiO₂ (101) diffractions in the right panel shows very limited peak shifts.

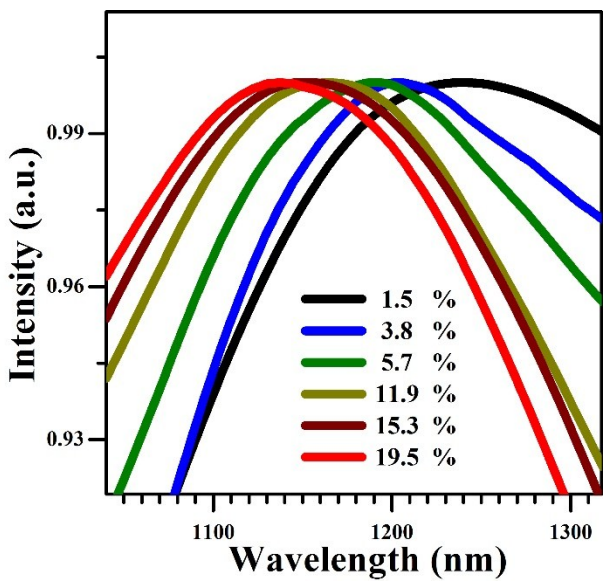


Fig. S9 Normalized LSPR peaks of W-doped TiO₂ NCs as a function of the dopant concentration.

Table S3. Chemical compositions of W-doped TiO₂ NCs prepared with different surfactant (OA and OLA) amounts.

Sample	Nominal W/Ti ratio (<i>atom</i> %)	W/Ti ratio from EDS (atom %)	Doping concentration from EDS (atom %)
0.5 mL OA	10	14.9	12.9
0.5 mL OA+0.1 mL OLA	10	13.9	12.2
0.5 mL OA+0.2 mL OLA	10	15.4	13.4
0.5 mL OA+0.4 mL OLA	10	15.1	13.3
0.5 mL OA+0.6 mL OLA	10	15.2	13.2
1 mL OA+0.6 mL OLA	10	16.4	14.1

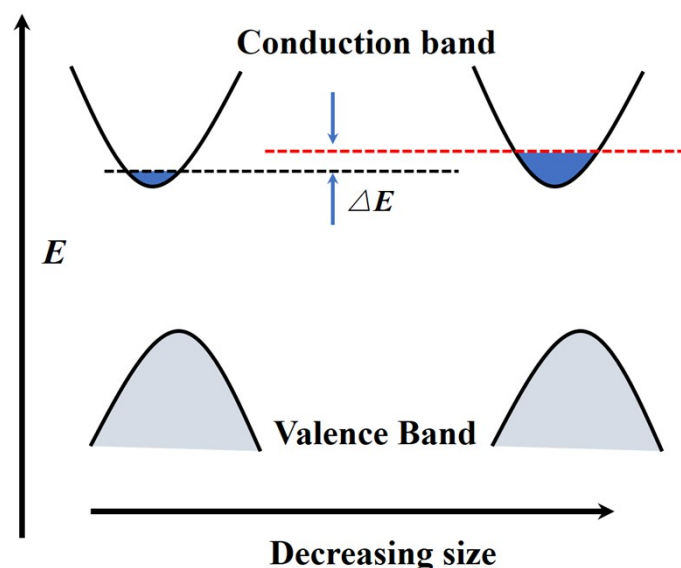


Fig. S10 Schematic energy diagram of W-doped TiO₂ with decreasing NC size showing the increase in intraband transition energy with the decrease in the NC size.

Table S4. Summary of the LSPR performance of metal oxide plasmonic NCs reported in the literature

Material	LSPR peak wavelength (nm)	Synthesis method	Ref.
Sn-doped In ₂ O ₃	1650-2600	Heat injection	8
			9
Sb-doped In ₂ O ₃	3100-5400	One-pot	10
Ti-doped In ₂ O ₃	4400-10333	One-pot	10
Ge-doped In ₂ O ₃	3500-4000	One-pot	11
Al-doped ZnO	2800-6200	Heat injection	12
Ga-doped ZnO	4273-6920	Heat injection	13
In-doped ZnO	> 2500	One-pot	14
Ge-doped ZnO	> 2500	Heat injection	15
In-doped CdO	2000-3200	One-pot	16
Sn-doped CdO	1252-3189	Heat injection	17
F, In co-doped CdO	1500-3300	One-pot	18
Sn-doped Zn-Cd-O	890-2600	Heat injection	19
CsWO ₃	700-1100	Heat injection	20
NaWO ₃	a broad peak around at 1112-1600	One-pot	21
Ga ₂ FeO ₄	1000-1300	One-pot	22
Nb-doped TiO ₂	> 2500	Heat injection	23
Nb-doped TiO₂	3300	One-pot	This work
W-doped TiO₂	980-1700	One-pot	This work
Mo-doped TiO₂	650	One-pot	This work

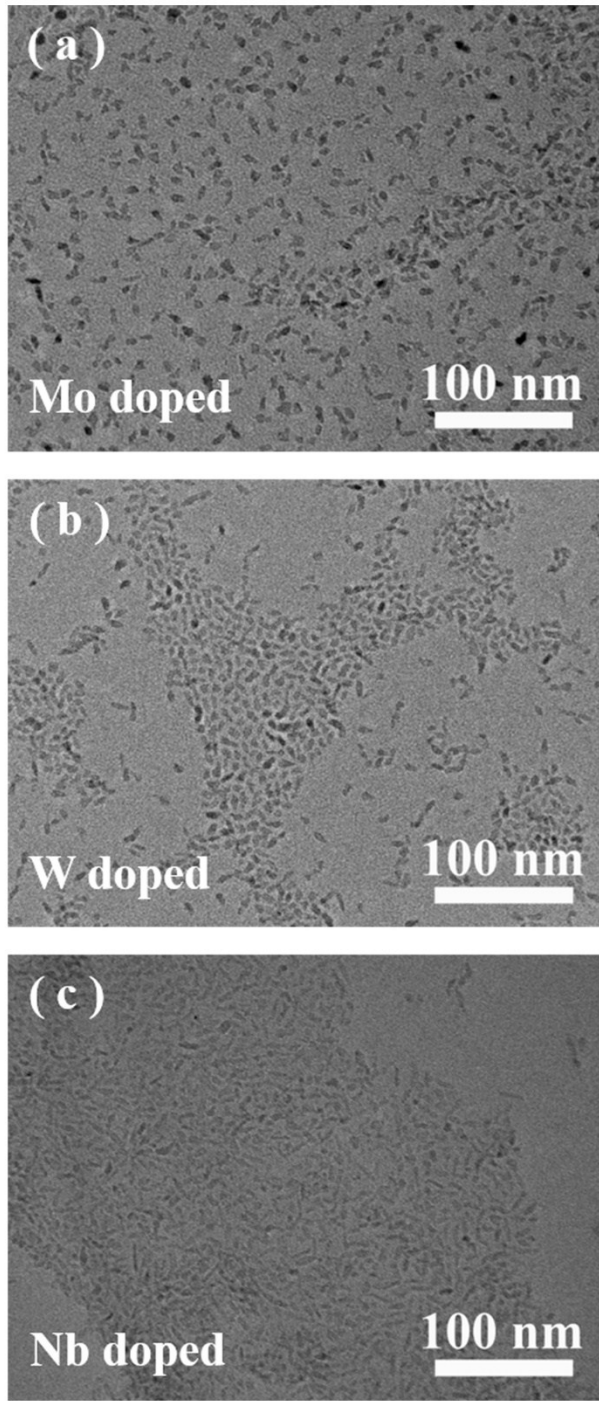


Fig. S11 TEM images of doped TiO_2 NCs from the gram-scale synthesis.

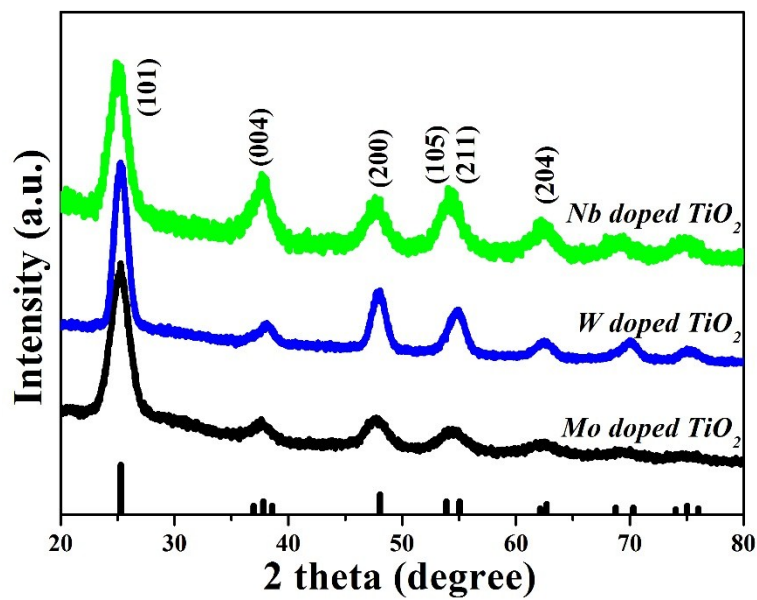


Fig. S12 XRD patterns of the doped TiO₂ NCs from the demonstrative scaled up synthesis. The reference reflections of anatase TiO₂ are shown on the 2 theta axis (JCPDS card 00-021-1272).

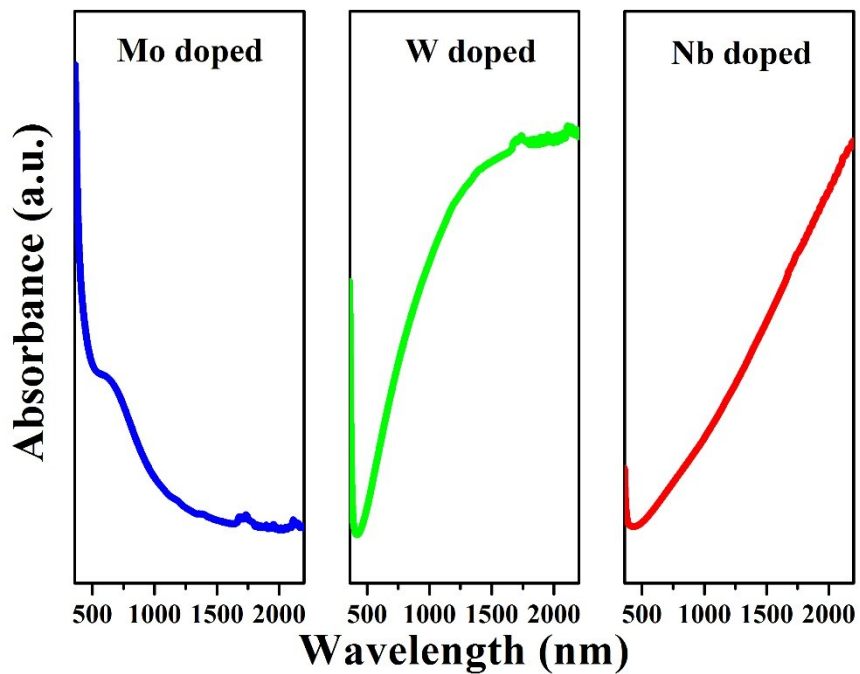


Fig. S13 UV-vis-IR absorption spectra of doped TiO_2 NCs from the gram-scale synthesis.

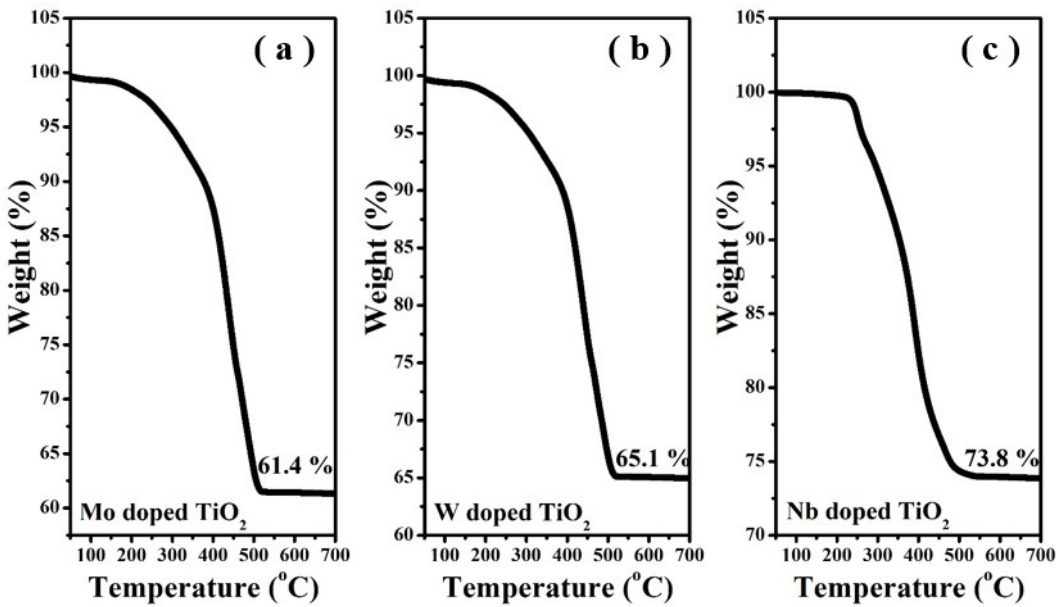


Fig. S14 TGA thermograms of doped TiO_2 NCs from the demonstrative scaled up synthesis. Theoretically, for 100% conversion of the precursors into doped NCs, 0.846, 0.934, and 0.843 g of Mo-, W-, and Nb-doped TiO_2 NCs should be formed. The actual yields of the demonstrative scaled up synthesis are therefore 86.4%, 86.6% and 91.1% for the Mo-, W-, and Nb-doped TiO_2 NCs respectively.

References

1. P. Qin, G. Fang, W. Ke, F. Cheng, Q. Zheng, J. Wan, H. Lei and X. Zhao, *J. Mater. Chem. A*, 2014, **2**, 2742-2756.
2. M. Vasilopoulou, A. Soultati, D. Georgiadou, T. Stergiopoulos, L. Palilis, S. Kennou, N. Stathopoulos, D. Davazoglou and P. Argitis, *J. Mater. Chem. A*, 2014, **2**, 1738-1749.
3. Y. E. Saleh, M. A. Gepreel and N. K. Allam, *Sci. Rep.*, 2017, **7**, 40291.
4. S. N. Svitashova and A. M. Gilinsky, *Appl. Surf. Sci.*, 2013, **281**, 109-112.
5. A. Agrawal, R. W. Johns and D. J. Milliron, *Annu. Rev. Mater. Res.*, 2017, **47**, 1-31.
6. Y. Liu, Y. Li and H. Zeng, *J. Nanomater.*, 2013, **2013**, 196521.
7. A. Kubacka, G. Colón and M. Fernández-García, *Catal. Today*, 2009, **143**, 286-292.
8. A. M. Schimpf, S. D. Lounis, E. L. Runnerstrom, D. J. Milliron and D. R. Gamelin, *J. Am. Chem. Soc.*, 2015, **137**, 518-524.
9. A. W. Jansons and J. E. Hutchison, *ACS Nano*, 2016, **10**, 6942-6951.
10. H. Fang, M. Hegde, P. Yin and P. V. Radovanovic, *Chem. Mater.*, 2017, **29**, 4970-4979.
11. E. L. Runnerstrom, A. Bergerud, A. Agrawal, R. W. Johns, C. J. Dahlman, A. Singh, S. M. Selbach and D. J. Milliron, *Nano Lett.*, 2016, **16**, 3390-3398.
12. R. Buonsanti, A. Llordes, S. Aloni, B. A. Helms and D. J. Milliron, *Nano Lett.*, 2011, **11**, 4706-4710.
13. M. Saha, S. Ghosh, V. D. Ashok and S. K. De, *Phys. Chem. Chem. Phys.*, 2015, **17**, 16067-16079.
14. E. Della Gaspera, A. S. R. Chesman, J. van Embden and J. J. Jasieniak, *ACS Nano*, 2014, **8**, 9154-9163.
15. E. Della Gaspera, N. W. Duffy, J. van Embden, L. Waddington, L. Bourgeois, J. J. Jasieniak and A. S. R. Chesman, *Chem. Commun.*, 2015, **51**, 12369-12372.
16. T. R. Gordon, T. Paik, D. R. Klein, G. V. Naik, H. Caglayan, A. Boltasseva and C. B. Murray, *Nano Lett.*, 2013, **13**, 2857-2863.
17. S. Ghosh, M. Saha, S. Paul and S. K. De, *Small*, 2017, **13**, 1602469.
18. X. Ye, J. Fei, B. T. Diroll, T. Paik and C. B. Murray, *J. Am. Chem. Soc.*, 2014, **136**, 11680-11686.
19. S. Ghosh, M. Saha, V. Dev Ashok, B. Dalal and S. De, *J. Phys. Chem. C*, 2015, **119**, 1180-1187.
20. J. Kim, A. Agrawal, F. Krieg, A. Bergerud and D. J. Milliron, *Nano Lett.*, 2016, **16**, 3879-3884.
21. J. Choi, K. Moon, I. Kang, S. Kim, P. J. Yoo, K. W. Oh and J. Park, *Chem. Eng. J.*, 2015, **281**, 236-242.
22. C. Urso, M. Barawi, R. Gaspari, G. Sirigu, I. Kriegel, M. Zavelani-Rossi, F. Scotognella, M. Manca, M. Prato, L. De Trizio and L. Manna, *J. Am. Chem. Soc.*, 2017, **139**, 1198-1206.
23. L. De Trizio, R. Buonsanti, A. M. Schimpf, A. Llordes, D. R. Gamelin, R. Simonutti and D. J. Milliron, *Chem. Mater.*, 2013, **25**, 3383-3390.